Hindawi
International Journal of RF and Microwave Computer-Aided Engineering
Volume 2024, Article ID 3897878, 13 pages
https://doi.org/10.1155/2024/3897878

Research Article

Design of Cross-Coupled Bandpass Filters with Flexible Coupling via Half-Mode Substrate-Integrated Waveguide

Qianwen Liu[1] **and Lei Zhu**[2]

[1]*Nanjing University of Posts and Telecommunications, College of Telecommunications and Information Engineering, Nanjing 210003, China*
[2]*University of Macau, Faculty of Science and Technology, Macau, SAR, China*

Correspondence should be addressed to Qianwen Liu; aliuqw@163.com

Received 14 October 2023; Revised 23 November 2023; Accepted 16 March 2024; Published 5 April 2024

Academic Editor: Vicente E. Boria

In this article, a simple approach for achievement of flexible coupling is presented based on the half-mode substrate-integrated waveguide (HMSIW). Since both electric and magnetic fields vary along the magnetic wall of the HMSIW, there exists mixed coupling between two adjacent HMSIWs. In this context, only by adjusting the width of the coupling slot at specific regions, both coupling property and strength can be conveniently controlled. Besides, as the coupling slot possesses the merits of simple structure and high flexibility, it is also expected to achieve desired couplings between multimode resonators. For demonstration, three cross-coupled bandpass filters (BPFs) with different kinds of frequency responses are constructed based on the typical cascaded trisection coupling topology by mixing one SIW and two HMSIWs, including two single-band and one dual-band designs. All measured results are highly consistent with the simulated ones, validating that the HMSIW not only has the inherent advantage of smaller size than the conventional SIW counterparts but also possesses unique feature in providing flexible coupling without extra circuit.

1. Introduction

The substrate-integrated waveguide (SIW) technology is attractive in the filter design due to its distinctive merits of low loss, high-quality factor, nice power handling capability, and easy integration. To satisfy the rapid development of modern communication systems, higher requirements have been put forward on the bandpass filters (BPFs) based on different forms of SIWs.

On one hand, with the demand for better anti-interference from adjacent frequency bands, filters with high frequency selectivity and stopband rejection are needed. In this context, the cross-coupled topology which is convenient to generate finite transmission zeros (TZs) has become attractive. As known, both positive and negative couplings are always required in the cross-coupled filters. Nevertheless, owing to the electric wall condition around the SIW, the positive coupling can be directly achieved with the inductive window whereas the realization of the negative coupling is comparatively difficult. To break the limitation of the electric wall condition, the most straightforward way is employing the stacked structure and then establishing coupling by etching slot in the common ground of adjacent SIWs [1]. However, the multilayered configuration is needed which will inevitably increase the fabrication complexity and error. Besides, in [2], although the SIWs are constructed in the same layer, an embedded short-ended strip line is adopted, and thus, the two-layer printed circuit board (PCB) process is also needed. To obtain negative coupling with the traditional single-layer PCB technique, a lot of coupling structures are put forward, such as coplanar lines [3], [4], interdigital slot-line (ISL) [5], shorted coplanar waveguide (CPW) [6], coupled stepped-impedance grounded CPWs (SIGCPWs) [7], H-shaped slot [8] or ring gap [9, 10] with shorted posts, a balanced microstrip line with a pair of plated through-holes [11, 12], and interdigital-like capacitive coupling structure [13]. However, these coupling structures are functioned together with the postwall iris which will

complicate the coupling structure. Moreover, most of them are focused on the coupling between single-mode SIWs.

On the other hand, dual-band BPFs are in high demand [14, 15]. To form one more operating passband, more resonances are necessary, and thus, a few effective methods have been put forward. The first one is introducing another group of resonators for another passband. Although this method is easy to be realized, the overall size of the circuit will be multiplied. The second one is combining other types of resonators with the SIW cavities, such as the back-to-back E-shaped DGS [16], E-shaped slotlines [17], CSRRs [18], and meander-line and composite right-/left-handed (CRLH) resonators [19]. Besides, in [20], a stepped-impedance resonator (SIR) BPF is designed and combined with the air-filled SIW BPF with circular cavities to obtain dual-band operation. Nevertheless, these additional resonators or circuits will increase the complexity of the entire filter and even affect the resonant property of the original SIWs. Under this circumstance, the multiple-mode SIW, which can provide more resonances without additional circuit, seems an attractive candidate. In [21–23], several resonant modes in a single cavity are exploited to realize dual passbands. However, perturbation elements are required to reallocate the resonances, and the attainable coupling structure is thus limited. Besides, dual-mode SIWs are widely used. In [4, 24, 25], the dominant and higher order modes in each SIW cavity are used to form dual passbands, but they are constructed based on the simplest cascaded topology. In [12, 26], although the cross-coupled structure is constructed, only two SIWs are working with two resonant modes. Moreover, to enhance the adjustability of the coupling structures, multilayered configurations are always adopted for dual-mode SIW filters [26, 27]. Consequently, it is still a challenge to design a planar cross-coupled dual-band BPF with simple structure and compact size.

In this article, the half-mode SIW (HMSIW) is studied and then applied for BPF designs. It is well known that both the width and area of the HMSIW are reduced by nearly half compared with the SIW [28, 29]. In fact, apart from the advantage in size, by fully utilizing the specific field distributions along the magnetic wall of the HMSIW, the coupling between two adjacent HMSIWs can be flexibly controlled without additional circuits. For demonstration, three cross-coupled filters are constructed, simulated, fabricated, and measured. The remainder of this article is organized as follows. In Section 2, resonant properties of the SIW and HMSIW are comprehensively investigated. In Section 3, two single-band filters are proposed based on two HMSIWs and one SIW. In Section 4, one dual-band BPF is constructed based on dual-mode resonators. In Section 5, comparative study with other reported SIW BPFs is presented. Finally, Section 6 draws a conclusion.

2. SIW and HMSIW

At the beginning, the fundamental resonators of SIW and HMSIW for construction of BPFs are fully investigated. Figure 1 depicts the configurations of the SIW and HMSIW, where the whole represents the top view of the SIW, while the grey half denotes the HMSIW. According to the cavity model theory, the electric and magnetic (EM) fields inside the rectangular SIW can be expressed in terms of TE_{m0n} [30], and the resonant frequency of TE_{m0n} mode can be calculated by

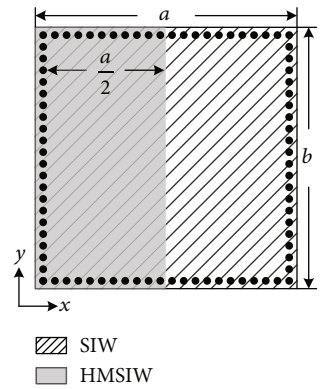

Figure 1: Configurations of SIW and HMSIW.

$$f_{\mathrm{TE}_{m0n}} = \frac{c}{2\sqrt{\mu_r \varepsilon_r}} \sqrt{\left(\frac{m}{a}\right)^2 + \left(\frac{n}{b}\right)^2}, \tag{1}$$

where c is the light velocity in vacuum, μ_r and ε_r are the relative permeability and permittivity, and m and n are the mode indices along the width and length, respectively.

Since the HMSIW is half a bisection of the SIW and equipped with one magnetic wall as shown in Figure 1, it can keep half of the even modes in the SIW. Herein, the first two even modes of the SIW, i.e., TE_{101} and TE_{102}, are studied. Figure 2 displays the computed electric and magnetic field distributions of these two modes, and the left or right half exactly represents the corresponding modes in the HMSIW which are denoted as half-TE_{101} and half-TE_{102}, respectively. As seen, both electric and magnetic fields vary along the magnetic wall of the HMSIW, and their field intensity ranges from 0 to maximum. In this context, since the coupling between the slot-coupled resonators is dependent on the slot width and the field along coupled edges, it can be expected to control the coupling between two adjacent HMSIWs only by reshaping the coupling slot.

3. Single-Band BPFs

In order to validate that the HMSIW has the potential to provide controllable electric and magnetic couplings, two single-band BPFs based on the typical cascaded trisection coupling topology shown in Figure 3 are constructed by virtue of two HMSIWs and one SIW in this section. Herein, both filters are working at the same frequency under the resonance of the fundamental mode of the HMSIW and SIW, while their TZs are located in the lower and upper stopbands, respectively. Specifically, the prescribed specifications are set as the center frequency of 5000 MHz, a bandwidth of 400 MHz, and an in-band return loss of 20 dB. Meanwhile,

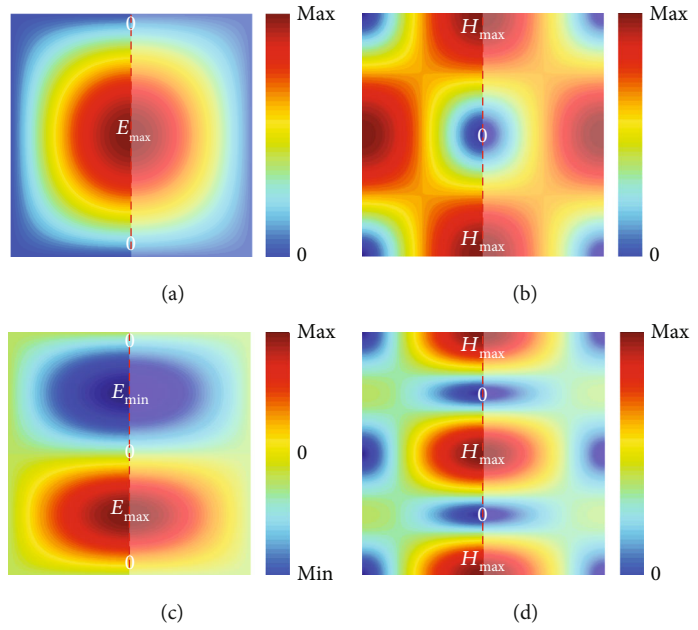

FIGURE 2: Computed field distributions of resonant modes in the SIW/HMSIW cavity: (a) electric and (b) magnetic fields of TE_{101}/half-TE_{101}; (c) electric and (d) magnetic fields of TE_{102}/half-TE_{102}.

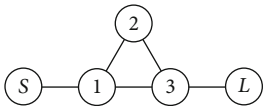

FIGURE 3: Coupling topology of the single-band BPF.

two TZs are separately located at 4500 or 5500 MHz, respectively. The substrate Rogers RO4003 with a permittivity of $\varepsilon_r = 3.55$ and a thickness of $h = 0.508$ mm is employed in all the presented designs. Besides, the full-wave electromagnetic (EM) simulator ANSYS HFSS is employed during the design procedure, and the fabricated circuits are measured by using the Agilent N5230A vector network analyzer.

3.1. One TZ in the Upper Stopband. The first demo is the filter with one TZ in the upper stopband. The targeted design parameters can be derived using the filtering network optimization synthesis procedure provided by CST Filter Design 3D as follows: $f_{01} = f_{03} = 4977$ MHz, $f_{02} = 5091$ MHz, $M_{12} = M_{23} = 0.076$, $M_{13} = 0.037$, and $Q_{S1} = Q_{L3} = 10.661$. It can be seen that all the coupling coefficients are positive, which should be realized with the magnetic couplings. Accordingly, the filter is constructed as detailed in Figure 4. As depicted, two HMSIWs correspond to R1 and R3, respectively, while the SIW for R2. The metallic pins surrounding the cavities are with the radius of 0.6 mm and a spacing of 0.2 mm. Then, the coupling between the SIW and HMSIWs is realized with the conventional coupling window, while that between two HMSIWs is even slot. Besides, two 50 Ω microstrip feeding lines with the strip width of $w_s = 1.15$ mm are connected and inserted into R1 and R3 along their midlines.

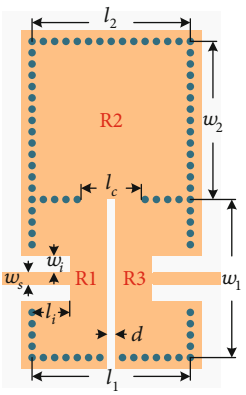

Parameters	Value (mm)
$l_1/l_2/w_2$	21.2
w_1	20.2
l_c	10.76
d	0.3
l_i	4.5
w_i	2.5
w_s	1.15

FIGURE 4: Configuration of the single-band BPF with one TZ in the upper stopband.

Next, the physical dimensions of the filter are found out based on the determined configuration and design parameters. The initial sizes of the SIW and HMSIW, which operate with TE_{101} and half-TE_{101}, respectively, can be calculated from (1) as $l_1 = l_2 = w_2 = 22.1$ mm and $w_1 = 23.2$ mm. Then, a full-wave EM simulation is carried out to extract the prescribed coupling coefficients and quality factor by using the following formulas [31]:

$$M_{ij} = \pm \frac{f_j^2 - f_i^2}{f_j^2 + f_i^2}, \qquad Q_e = \frac{\omega_0}{\Delta\omega_{\pm 90^\circ}}. \tag{2}$$

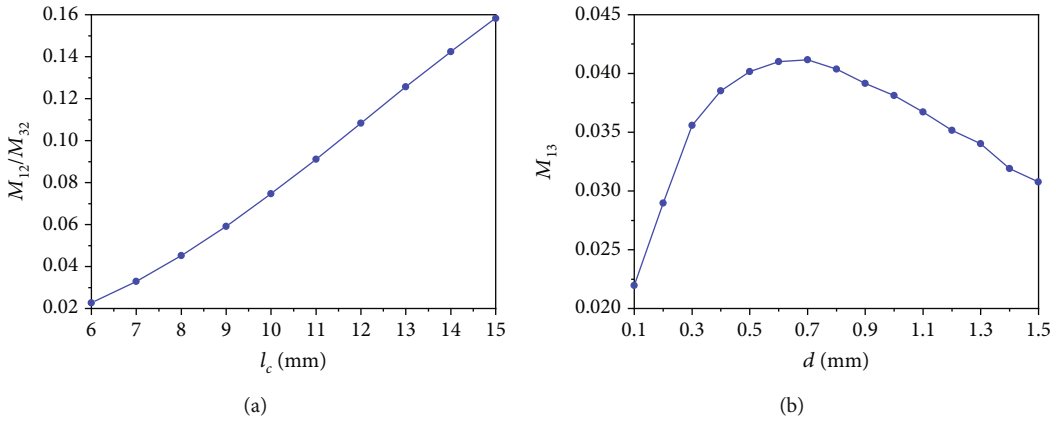

FIGURE 5: Extracted coupling coefficients for the single-band BPF with one TZ in the upper stopband: (a) M_{12}/M_{32} versus l_c; (b) M_{13} versus d.

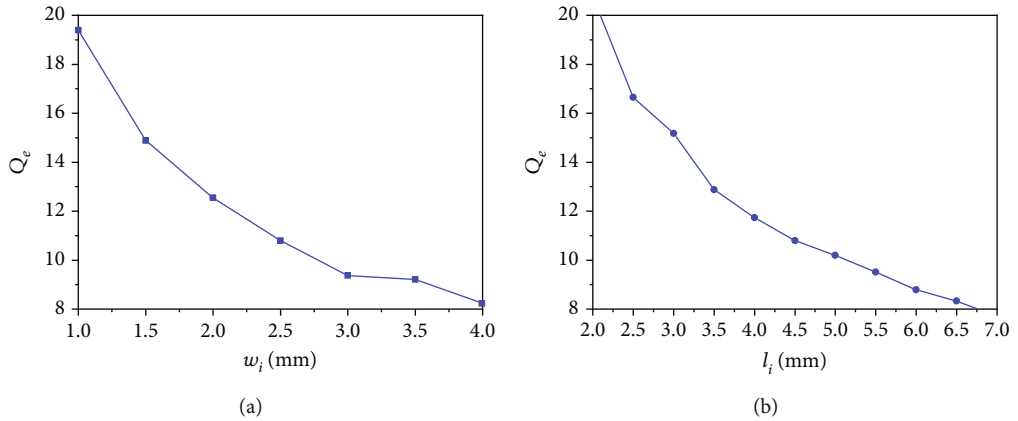

FIGURE 6: Extracted quality factor Q_e for the single-band BPF with one TZ in the upper stopband: (a) w_i; (b) l_i.

In this filter, the coupling between R1/R3 and R2 (M_{12}/M_{32}) is adjusted simultaneously by changing the coupling window's width l_c and that between R1 and R3 (M_{13}) is determined from the slot width d. Figure 5 plots the extracted coupling coefficients versus relevant geometrical dimensions. As depicted, with the increase of l_c, M_{12}/M_{32} gets improved monotonically. Besides, owing to the specific field distribution along the coupling edges of the HMSIWs, M_{13} does not vary monotonically but firstly rises up and then falls down with d. Accordingly, to meet the design parameters, the initial dimensions in coupling structures are estimated as $l_c = 10.1$ mm and $d = 0.33$ mm. The extracted quality factor Q_e is determined from the slot length l_i and slot width w_i of the inserted feeding line. From the extracted curves in Figure 6, it can be observed that Q_e decreases against both w_i and l_i. To ease the design, w_i is directly fixed as 2.5 mm, and then, l_i can be evaluated as 4.52 mm.

Based on the initial dimensions, a fine tuning is employed on the entire filter to optimize the filter performance. The final dimensions of the filter are listed in Figure 4. The designed filter is finally fabricated and measured. Figure 7 shows the photography of the fabricated filter, and Figure 8 depicts the simulated and measured

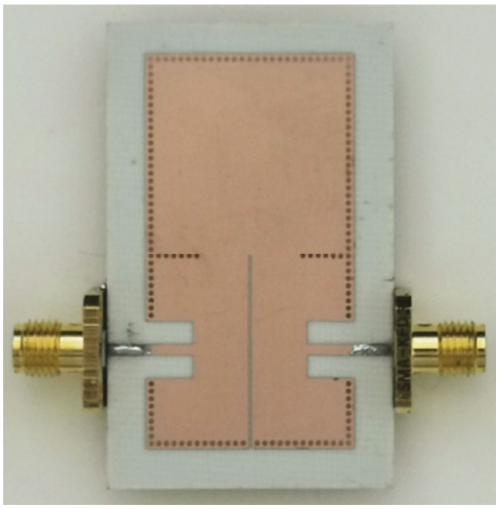

FIGURE 7: Photography of the fabricated single-band BPF with one TZ in the upper stopband.

frequency responses. The measured results are in high accordance with the simulated ones, demonstrating a 3 dB fractional bandwidth of 14.48% with the center frequency of

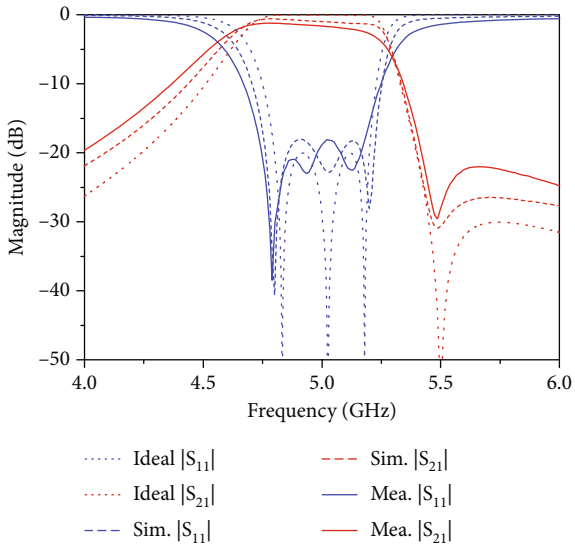

FIGURE 8: Ideal, simulated, and measured results of the single-band BPF with one TZ in the upper stopband.

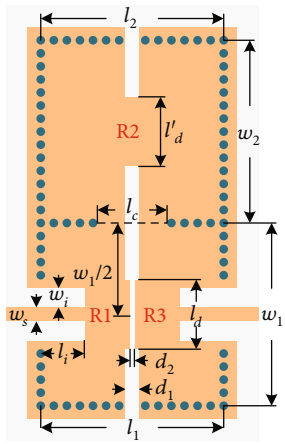

Parameters	Value (mm)
$l_1/l_2/w_2$	22.2
w_1	16.8
l_c	11.64
l_d	9
d_1	2.5
d_2	0.2
l_i	4.5
w_i	2.5
w_s	1.15

FIGURE 9: Configuration of the single-band BPF with one TZ in the lower stopband.

4.9 GHz. The minimum insertion loss within the passband is 1.22 dB, and the TZ appears at 5.49 GHz.

3.2. One TZ in the Lower Stopband. The second demo is the filter with one TZ in the lower stopband. The targeted design parameters are found as follows: $f_1 = f_3 = 5021$ MHz, $f_2 = 4920$ MHz, $M_{12} = M_{23} = 0.077$, $M_{13} = -0.033$, and $Q_{S1} = Q_{L3} = 10.664$. Notably, the coupling coefficient M_{13} is transformed to be negative in this case. Given this, the coupling structure between R1 and R3, i.e., two HMSIWs, must be properly modified. As displayed in Figures 2(a) and 2(b), the electric field of half-TE_{101} along the magnetic wall is the strongest at the middle and gradually gets reduced towards both sides while the magnetic field performs the reverse trend. Given this, the coupling slot between R1 and R3 is no longer even but narrowed in the middle region and widened at both sides as shown in Figure 9, so as to

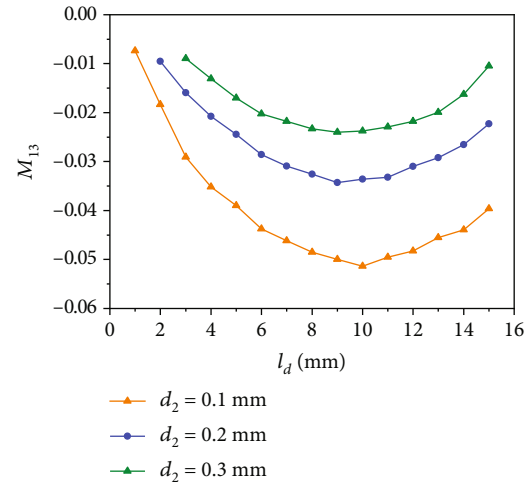

FIGURE 10: Extracted coupling coefficient of M_{13} versus the slot length l_d with the width d_2 as a parameter for the single-band BPF with one TZ in the lower stopband.

enhance the electric coupling while reduce the magnetic ones. In addition, as the slot at two sides is very wide, two symmetrical slots are etched in the SIW to ensure the similar field at two sides of the coupling window between the HMSIWs and SIW. The width of the slots in the SIW is d_1, which is same as that of the coupling slot in two sides between HMSIWs. Besides, the distance between the slots is determined from the relative sizes of the HMSIW and SIW as well as the slot length between HMSIW with $l'_d = w_2/w_1 \cdot l_d$.

Similarly, the dimensions of the filter are then investigated. Firstly, the dimensions of the resonators are calculated from (1) as $l_2 = w_2 = l_1 = 22.9$ mm and $w_1 = 22.0$ mm. Besides, as the same feeding structure and coupling window of the first design example are adopted and the corresponding targeted coupling coefficients and quality factor are approximately equal, the same initial dimensions are roughly evaluated herein. Afterwards, the coupling slot is studied. According to the above analysis, the slot width in the middle should be much smaller than that in two sides to provide relatively stronger electric coupling. Given this, to reduce variables in the coupling slot, d_1 is readily fixed as 2.5 mm and then d_2 and l_d are investigated as plotted in Figure 10. As depicted, the coupling strength $|M_{13}|$ gets enhanced with narrower slot width d_2 when the length l_d is fixed. Besides, it firstly gets improved and then reduced as the length l_d increases, and it always eventually reaches maximum around 9 mm, indicating that the rate of change in magnetic coupling becomes higher than that of the electric ones when l_d exceeds 9 mm. As such, the initial dimensions of the coupling slot are figured out as $l_d = 8.6$ mm, $d_1 = 2.5$ mm, and $d_2 = 0.2$ mm.

After fine tuning, the final dimensions are all obtained as tabulated in Figure 9. The photography of the fabricated circuit is shown in Figure 11, while the simulated and measured results of the filter are provided in Figure 12. The simulated and measured results are in good agreement,

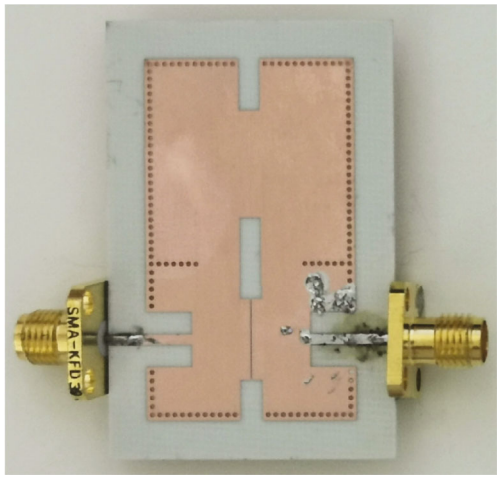

Figure 11: Photography of the fabricated single-band BPF with one TZ in the lower stopband.

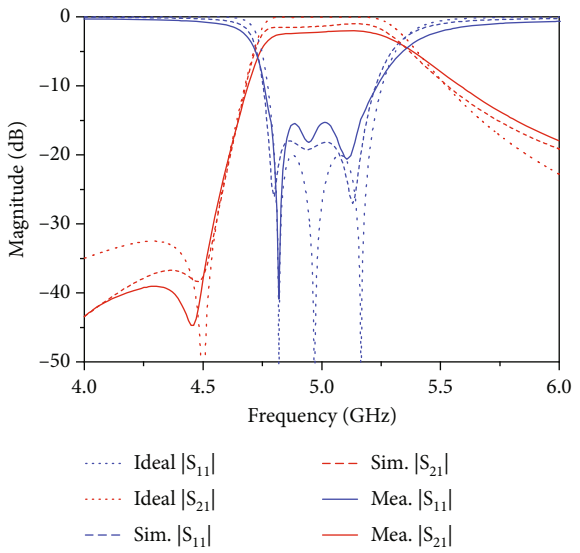

Figure 12: Ideal, simulated, and measured results of the single-band BPF with one TZ in the lower stopband.

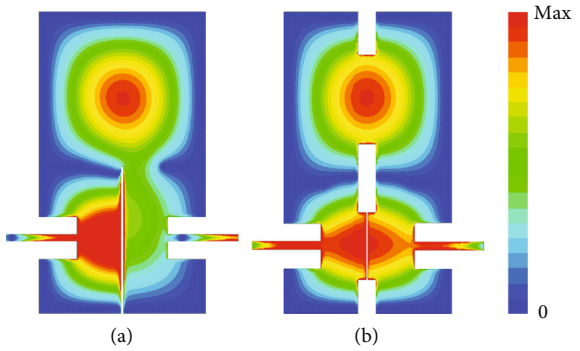

Figure 13: Simulated electric field distributions of the single-band BPFs at their respective center frequencies: (a) BPF with one TZ in the upper stopband; (b) BPF with one TZ in the lower stopband.

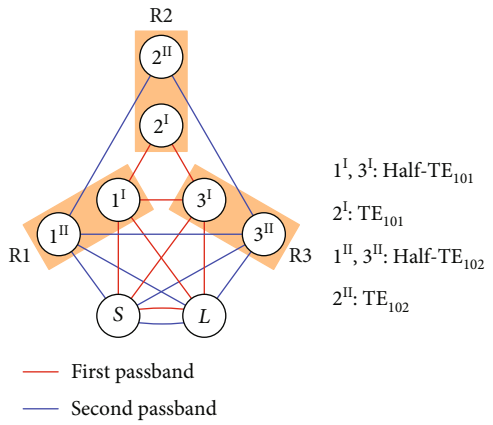

Figure 14: Coupling topology of the dual-band BPF.

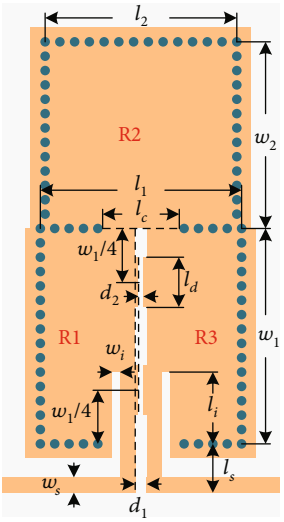

Parameters	Value (mm)
l_1	21.7
w_1	23
l_2	21
w_2	19.5
l_c	12.6
d_1	0.4
d_2	1.2
l_d	5
l_i	7.8
w_i	0.8
l_s	6
w_s	1.15

Figure 15: Configuration of the dual-band BPF.

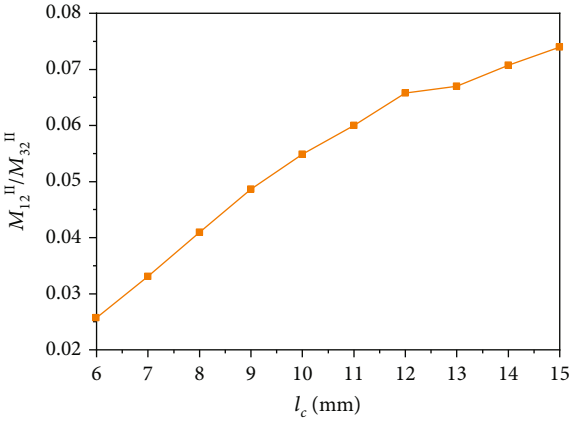

Figure 16: Extracted coupling coefficients of $M_{12}{}^{II}/M_{23}{}^{II}$ between the TE_{102}-mode SIW and half-TE_{102}-mode HMSIW for the dual-band BPF.

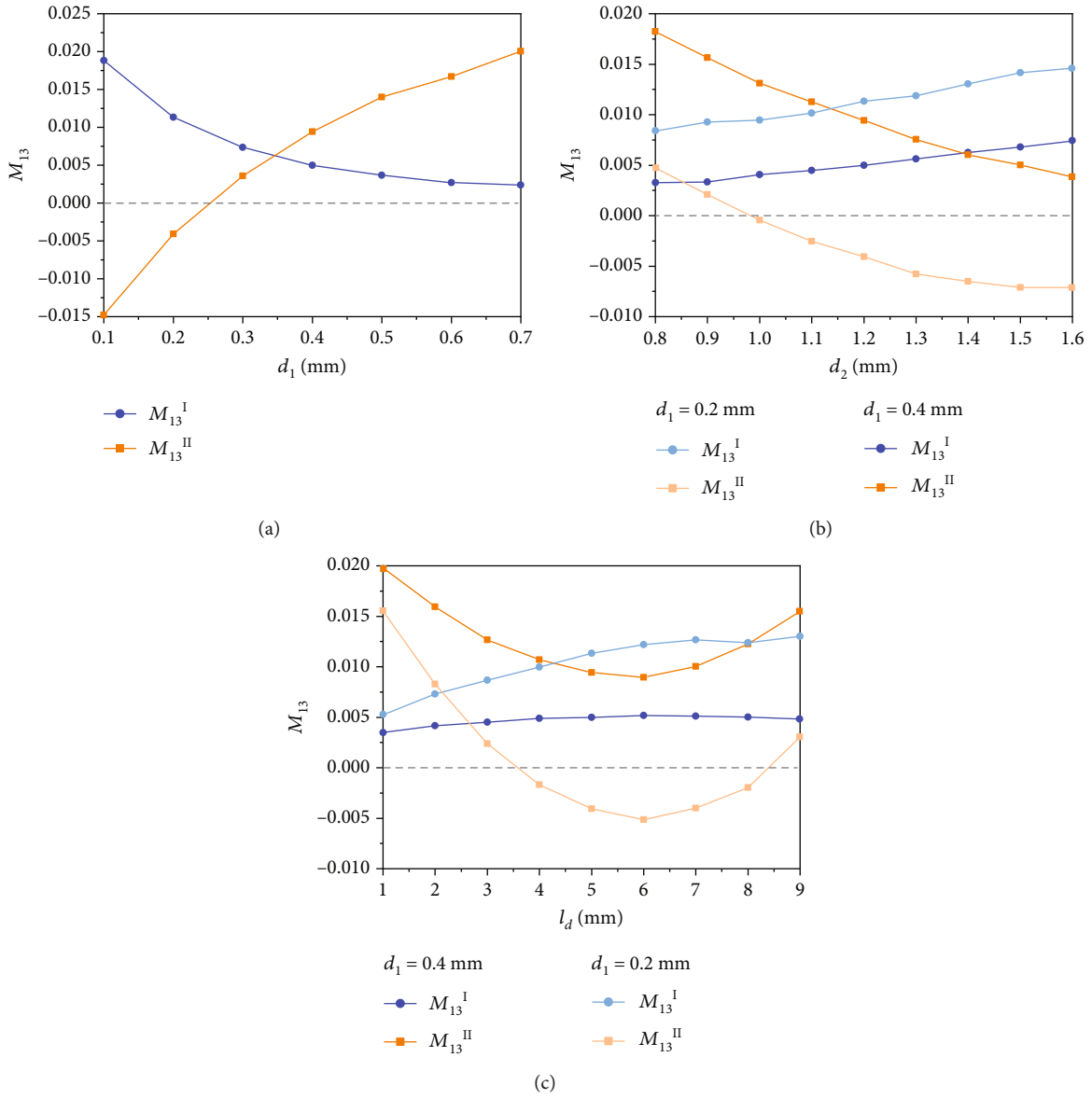

FIGURE 17: Extracted coupling coefficients between two HMSIWs of the dual-band BPF: (a) k_{13} versus d_1; (b) k_{13} versus d_2; (c) k_{13} versus l_d.

and the measured center frequency, 3 dB fractional bandwidth, and minimum insertion loss are 5.06 GHz, 12.65%, and 1.92 dB, respectively. Additionally, the TZ appears at 4.45 GHz.

Figure 13 displays the electric field distributions of the two single-band BPFs at their respective center frequencies, and their distinctive features well verify that resonant modes of TE_{101} and half-TE_{101} are indeed effectively excited in these two designs.

4. Dual-Band BPF

Apart from providing different coupling property and strength under the same resonant modes for design of single-band BPFs with different performances, the proposed coupling scheme can also be further applied to realize proper couplings between dual-mode HMSIWs. For demonstration, a dual-band BPF is presented based on the first two resonant modes of TE_{101} and TE_{102} in the SIW together with their corresponding modes of half-TE_{101} and half-TE_{102} in the HMSIW. The prescribed specifications are the center frequencies of 5000 and 8000 MHz with the bandwidths of 530 and 1200 MHz for the first and second passbands, respectively. Besides, three TZs are placed at 3450, 4350, and 5550 MHz around the first passband, while three are 8900, 9200, and 9700 MHz around the second one. The so-obtained coupling topology is shown in Figure 14, where the superscript I and II denote the first and second resonant modes in each resonator, which dominate the first and second passbands, respectively. Besides, apart from the same cascaded trisection coupling structure of the single-band designs, extra cross coupling paths of source to load, source

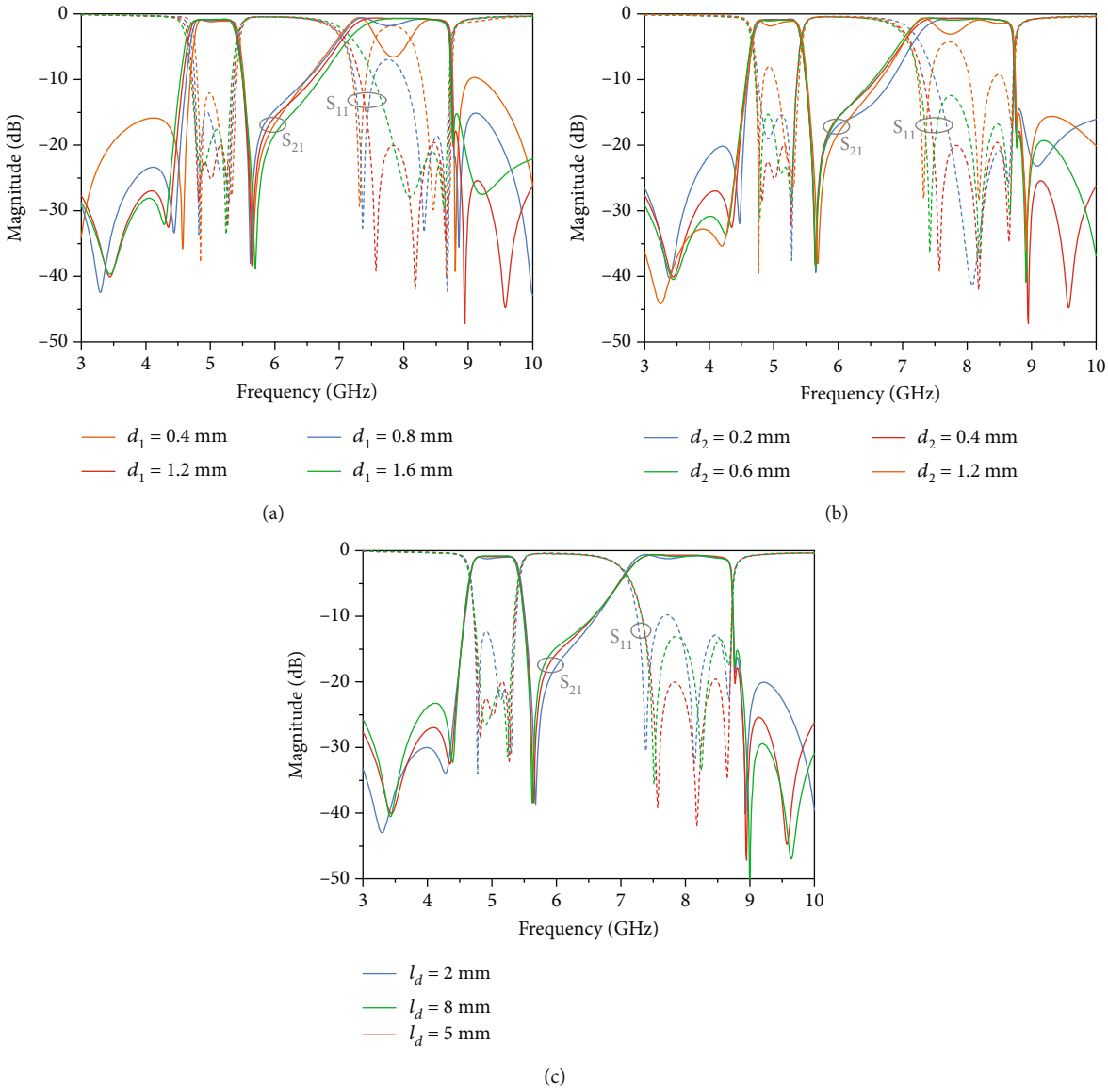

Figure 18: Frequency responses of the dual-band BPF varying with the dimensions in the coupling slot: (a) d_1; (b) d_2; (c) l_d.

to resonator 3, and load to resonator 1 are introduced to generate more TZs for better out-of-band performances. Correspondingly, the design parameters can be obtained as follows: $f_{01}{}^{\mathrm{I}} = f_{03}{}^{\mathrm{I}} = 4987$ MHz, $f_{02}{}^{\mathrm{I}} = 5035$ MHz, $M_{12}{}^{\mathrm{I}} = M_{23}{}^{\mathrm{I}} = 0.111$, $M_{13}{}^{\mathrm{I}} = 0.006$, $Q_{S1}{}^{\mathrm{I}} = Q_{L3}{}^{\mathrm{I}} = 7.797$, $Q_{S3}{}^{\mathrm{I}} = Q_{L1}{}^{\mathrm{I}} = 326.435$, and $M_{SL}{}^{\mathrm{I}} = 0.0051$ and $f_{01}{}^{\mathrm{II}} = f_{03}{}^{\mathrm{II}} = 8610$ MHz, $f_{02}{}^{\mathrm{II}} = 8635$ MHz, $M_{12}{}^{\mathrm{II}} = M_{23}{}^{\mathrm{II}} = 0.066$, $M_{13}{}^{\mathrm{II}} = -0.065$, $Q_{S1}{}^{\mathrm{II}} = Q_{L3}{}^{\mathrm{II}} = 3.401$, $Q_{S3}{}^{\mathrm{II}} = Q_{L1}{}^{\mathrm{II}} = 28.935$, and $M_{SL}{}^{\mathrm{II}} = -0.096$.

Based on the coupling topology and design parameters, the dual-band BPF is constructed as shown in Figure 15. As seen, the coupling between adjacent SIW (R2) and HMSIWs (R1 and R3) is implemented by the coupling window just like the above two single-band designs. The design curve of $M_{12}{}^{\mathrm{I}}/M_{23}{}^{\mathrm{I}}$ is the same as that for the single-band designs in Figure 5(a), and that of $M_{12}{}^{\mathrm{II}}/M_{23}{}^{\mathrm{II}}$ is given in Figure 16. Accordingly, the coupling width l_c can be roughly estimated as 11 mm. Then, the coupling slot is studied. Herein, the coupling property between two HMSIWs is inverse in two passbands, that is, positive for the first passband and negative for the second one, so the shape of the coupling slot should be adjusted based on the field distributions of both resonant modes. As depicted in Figure 2, the electric field of half-TE_{101} along the magnetic wall is maximum at the middle while that of half-TE_{102} is in the upper and bottom one quarter. Accordingly, with the analysis of the coupled half-TE_{101}-mode HMSIWs in the above section, the width of the coupling slot around its upper and bottom one quarter is set to be narrower. Figure 17 shows the extracted coupling coefficients of $M_{13}{}^{\mathrm{I}}$ and $M_{13}{}^{\mathrm{II}}$ versus all dimensions in the coupling slot, and it can be easily found

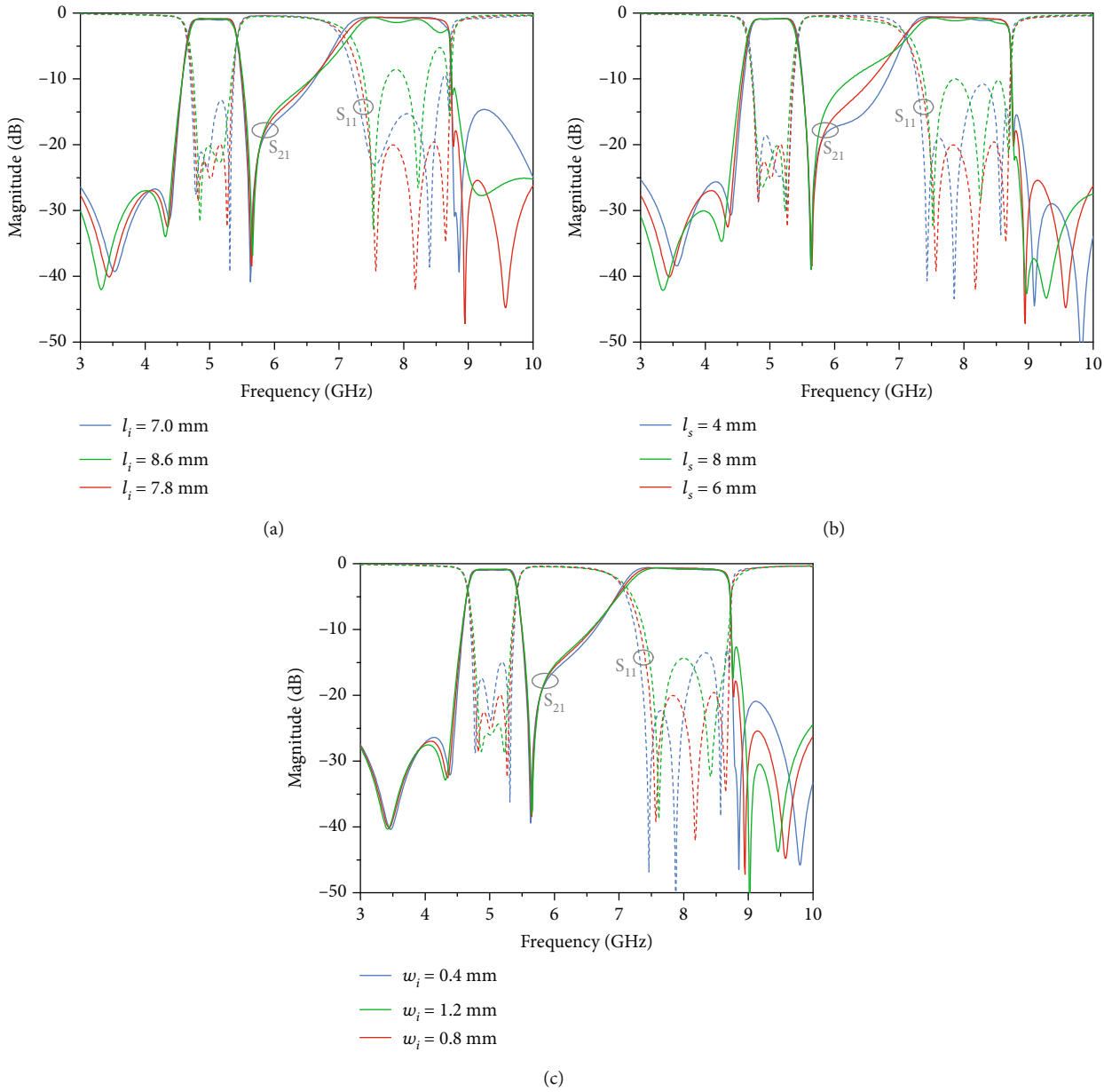

Figure 19: Frequency responses of the dual-band BPF varying with the dimension in the feeding lines: (a) l_i; (b) l_s; (c) w_i.

that $M_{13}{}^{\mathrm{II}}$ is much more sensitive to the dimensional variations. As depicted in Figure 17(a), as the width of the narrow part of the coupling slot d_1 decreases, the coupling coefficient of half-TE_{101} is enhanced and keeps positive, while that of half-TE_{102} is reduced from positive to negative. Figures 17(b) and 17(c) study the other two dimensions of d_2 and l_d of the coupling slot with d_1 as a parameter. As seen, $M_{13}{}^{\mathrm{I}}$ gets improved with the increase of both d_2 and l_d. Meanwhile, $M_{13}{}^{\mathrm{II}}$ decreases against d_2, and it firstly declines and then rises against l_d. Moreover, when d_1 is reduced to a certain value, $M_{13}{}^{\mathrm{II}}$ is switched between the positive and negative couplings. At last, the feeding structure is investigated. As shown in Figure 15, the feeding lines are shifted to the coupling slot between R1 and R3 to establish the cross couplings among R1, R3, input, and output ports. In this context, couplings of M_{13} and M_{SL} together with quality factors of Q_{S1}/Q_{L3} and Q_{L1}/Q_{S3} depend on both feeding structures and coupling slot, and thus, the relative dimensions are directly obtained from the frequency responses as shown in Figures 18 and 19. As seen, the coupling slot and feeding structure codetermine both in-band and out-of-band performances, and they have a greater impact on the frequency responses of the second passband as expected.

After optimization, the final dimensions are achieved as given in Figure 15. Figure 20 shows the simulated electric field distributions in this filter in both passbands. As observed, the first resonant modes of TE_{101} and half-TE_{101}

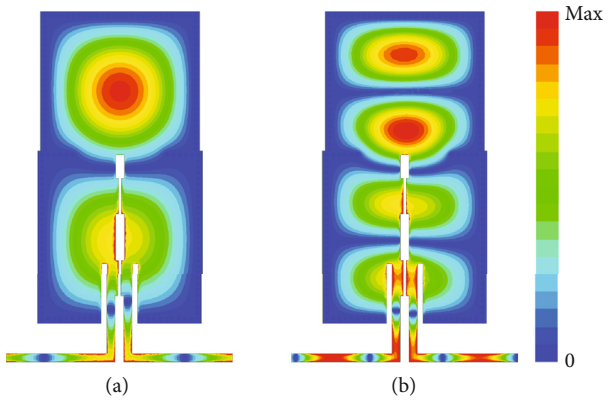

FIGURE 20: Simulated electric field distributions in the dual-band BPF: (a) the first passband; (b) the second passband.

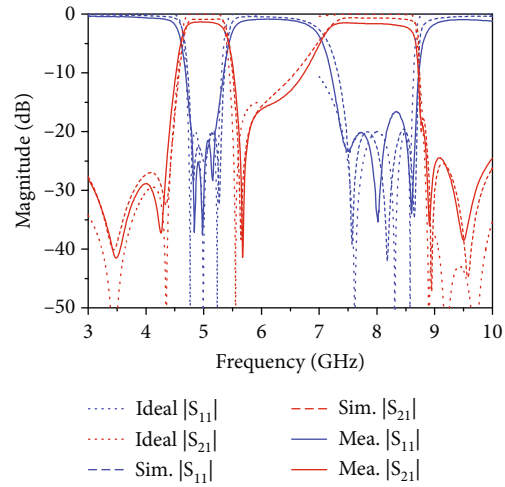

FIGURE 22: Ideal, simulated, and measured results of the dual-band BPF.

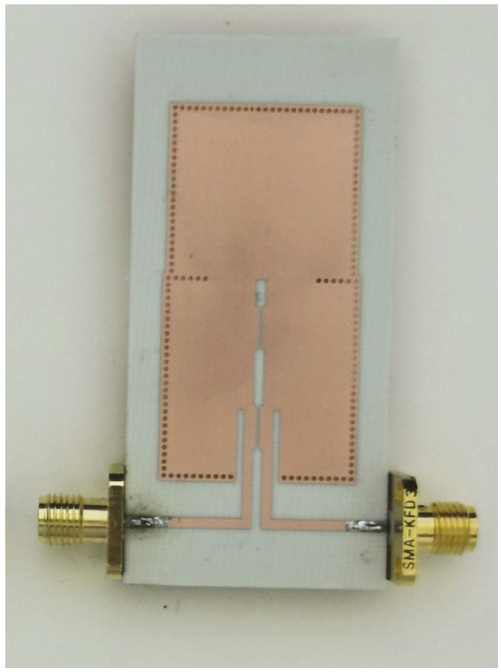

FIGURE 21: Photography of the fabricated dual-band BPF.

of the SIW and HMSIW form the first passband, while TE_{102} and half-TE_{102} contribute to the second passband. Figure 21 displays the photography of the fabricated circuit, while Figure 22 shows the simulated and measured results. The measured results indicate that the center frequencies of two working bands are 5.02 and 7.85 GHz with 3 dB fractional bandwidths of 15.84% and 20.64%, respectively. The minimum insertion losses within these two passbands are 1.34 and 1.47 dB. Six TZs located at 3.48, 4.26, 5.67, 8.77, 8.91, and 9.50 GHz result in a nice stopband performance. Herein, it should be mentioned that owing to the utilization of the higher order mode for the upper passband, the circuit size of the dual-band filter is $0.719\lambda_g \times 1.542\lambda_g$, which is slight larger than that of the single-band ones, which are $0.703\lambda_g \times 1.338\lambda_g$ and $0.735\lambda_g \times 1.262\lambda_g$. Moreover, the footprint of the SIWs is not enlarged, and the increasement on the overall size is resulted from the feeding lines.

5. Discussion

To highlight the advantages of the proposed design scheme, comprehensive comparison with other reported SIW filters is presented in Table 1. As seen, the proposed coupling scheme has the unique ability to provide the mixed coupling without extra circuit, while those in other designs are realized by virtue of additional coupling structures [7, 13] or other types of resonators [6]. Besides, even if there is no need of negative coupling, extra circuits are also required. In [32], a microstrip line section is used to connect the two doublets. In [21], a segment of CPW is required to connect the two cavities to serve a cascading function as nonresonant nodes (NRNs). Apart from the structural advantage, compared with the above-mentioned filters, the proposed filters can achieve much wider bandwidth with smaller size and lower profile. Compared with the designs in [22], our proposed ones provide significantly wider bandwidth based on the simple single-layer configuration. Compared to the design in [33], both size and profile are highly reduced in our proposed filters and the bandwidth is also much wider. As for the designs in [19], two different types of microstrip line resonators are introduced at the cost of the increased design complexity. In summary, the proposed filters have attained attractive advantages in both configuration and performances.

6. Conclusion

In this article, a simple approach for achievement of flexible coupling is firstly presented based on the HMSIWs. Attributing to the specific field distributions along the magnetic wall of the HMSIW, the coupling between two HMSIW can be flexibly and conveniently controlled only by modifying the shape of the coupling slot. On this basis, three bandpass filters with different kinds of frequency responses are

Table 1: Comparison with other reported SIW BPFs.

Ref.	Technique	Negative coupling	Additional coupling structure	Layers	Np	Nz	f_0 (GHz)	FBW (%)	IL (dB)	Size (λ_g^2)	Profile (λ_g)
[6]	SIW+shorted CPW	Y	N	1	5	4	7.5	5.2	2.2	1.09	0.025
[7]	SIW+SIGCPW	Y	Y	1	3	2	9.96	4.07	1.64	1.25	0.025
[13]	SIW+HMSIW	N	N	1	3/3	2	5/7.5	5.46/4.75	1.65/2.25	1.53	0.014
	HMSIW	Y	Y		4/4	4	5/8.5	6.26/7.75	2.02/1.82	1.10	0.016
[19]	SIW+CRLH+meander-line	N	N	1	5	2	10.14	12.9	0.91	0.63	0.025
[21]	Multimode circular SIW	N	Y	1	5/5	4	46.7/60	11.7/6.8	2/2.8	2.91	—
[22]	Multimode folded SIW	N	N	2	3	3	10.18	3.2	2.33	0.76	0.026
					2/2	4	8.71/10.1	1.9/2.7	2.8/1.98	0.76	0.022
					4	4	10.08	4.5	1.82	0.77	0.025
[32]	Multimode HMSIW	N	Y	1	4	4	10	5.3	2.4	1.75	0.025
[33]	Multimode SIW	N	N	1	5	2	10	3.5	2.04	3.77	0.025
This work	SIW+HMSIW	Y	N	1	3	1	4.90	14.48	1.22	0.94	0.016
						1	5.06	12.65	1.92	0.93	
	Dual-mode SIW+dual-mode HMSIW				3/3	6	5.02/7.85	15.84/20.64	1.34/1.47	1.11	

f_0: center frequency; FBW: fractional bandwidth; IL: insertion loss; Np: number of transmission poles; Nz: number of TZs; Layers: number of substrate layers; λ_g: guided wavelength in the dielectric substrate at the center frequency of the passband or the first passband of the multiband.

constructed, simulated, and fabricated. All measured results are in high agreement with their corresponding simulated ones, thereby validating the effectiveness of the proposed coupling scheme. Moreover, the proposed filters have the attractive features of simple configuration and compact size. Moreover, there is no doubt that the coupling scheme is also applicable for realization of other coupling topologies, which indicates that the proposed design method applies for various practical applications. Consequently, it can be reasonably concluded that the proposed design method is a feasible and promising candidate in advanced SIW filter designs.

Data Availability

The data used to support the findings of this study are included within the article.

Conflicts of Interest

The authors declare that there is no conflict of interest regarding the publication of this paper.

Acknowledgments

This work was supported in part by the National Natural Science Foundation of China under Grant nos. 62101279 and 61971475 and in part by Nanjing University of Posts and Telecommunications Scientific Foundation (NUPTSF) under Grant nos. NY221010 and NY217002.

References

[1] K.-S. Chin, C.-C. Chang, C.-H. Chen, Z. Guo, D. Wang, and W. Che, "LTCC multilayered substrate-integrated waveguide filter with enhanced frequency selectivity for system-in-package applications," *IEEE Transactions on Components, Packaging and Manufacturing Technology*, vol. 4, no. 4, pp. 664–672, 2014.

[2] K. Gong, W. Hong, Y. Zhang, P. Chen, and C. J. You, "Substrate integrated waveguide quasi-elliptic filters with controllable electric and magnetic mixed coupling," *IEEE Transactions on Microwave Theory and Techniques*, vol. 60, no. 10, pp. 3071–3078, 2012.

[3] B. Potelon, J.-F. Favennec, C. Quendo, E. Rius, C. Person, and J.-C. Bohorquez, "Design of a substrate integrated waveguide (SIW) filter using a novel topology of coupling," *IEEE Microwave and Wireless Components Letters*, vol. 18, no. 9, pp. 596–598, 2008.

[4] A. R. Azad and A. Mohan, "Substrate integrated waveguide dual-band and wide-stopband bandpass filters," *IEEE Microwave and Wireless Components Letters*, vol. 28, no. 8, pp. 660–662, 2018.

[5] W. Shen, L.-S. Wu, X.-W. Sun, W.-Y. Yin, and J.-F. Mao, "Novel substrate integrated waveguide filters with mixed cross coupling (MCC)," *IEEE Microwave and Wireless Components Letters*, vol. 19, no. 11, pp. 701–703, 2009.

[6] P. Chu, P. Zhu, J. Feng et al., "Substrate integrated waveguide filter with flexible mixed coupling," *IEEE Transactions on Microwave Theory and Techniques*, vol. 71, no. 9, pp. 4003–4011, 2023.

[7] Q. Liu, D. Zhou, D. Zhang, and D. Lv, "A novel frequency-dependent coupling with flexibly controllable slope and its applications on substrate-integrated waveguide filters," *IEEE Microwave and Wireless Components Letters*, vol. 28, no. 11, pp. 993–995, 2018.

[8] C. J. You, Z. N. Chen, X. W. Zhu, and K. Gong, "Single-layered SIW post-loaded electric coupling-enhanced structure and its filter applications," *IEEE Transactions on Microwave Theory and Techniques*, vol. 61, no. 1, pp. 125–130, 2013.

[9] A. Anand and X. Liu, "Reconfigurable planar capacitive coupling in substrate-integrated coaxial-cavity filters," *IEEE Transactions on Microwave Theory and Techniques*, vol. 64, no. 8, pp. 2548–2560, 2016.

[10] B.-S. Zhang, X.-W. Zhu, X.-L. Yang, and X. Liu, "A sixth-order SIW bandpass filter based on combining single- and dual-mode cavities with high selectivity at Ka-band," *International Journal of RF and Microwave Computer-Aided Engineering*, vol. 32, no. 7, 2022.

[11] M.-H. Ho, J.-C. Li, and Y.-C. Chen, "Miniaturized SIW cavity resonator and its application in filter design," *IEEE Microwave and Wireless Components Letters*, vol. 28, no. 8, pp. 651–653, 2018.

[12] K. Zhou, C.-X. Zhou, and W. Wu, "Resonance characteristics of substrate-integrated rectangular cavity and their applications to dual-band and wide-stopband bandpass filters design," *IEEE Transactions on Microwave Theory and Techniques*, vol. 65, no. 5, pp. 1511–1524, 2017.

[13] K. Zhou, C.-X. Zhou, and W. Wu, "Dual-mode characteristics of half-mode SIW rectangular cavity and applications to dual-band filters with widely separated passbands," *IEEE Transactions on Microwave Theory and Techniques*, vol. 66, no. 11, pp. 4820–4829, 2018.

[14] R. Mu, Y. Wu, L. Pan, W. Zhao, and W. Wang, "A miniaturized low-loss switchable single- and dual-band bandpass filter," *International Journal of RF and Microwave Computer-Aided Engineering*, vol. 2023, Article ID 9025980, 8 pages, 2023.

[15] Y. Zheng, Z. Wang, and Y. Dong, "Compact, dual-band, and hybrid filter based on combline and substrate integrated waveguide resonators," *International Journal of RF and Microwave Computer-Aided Engineering*, vol. 32, no. 1, 2022.

[16] S. Xu, K. Ma, F. Meng, and K. S. Yeo, "Novel defected ground structure and two-side loading scheme for miniaturized dual-band SIW bandpass filter designs," *IEEE Microwave and Wireless Components Letters*, vol. 25, no. 4, pp. 217–219, 2015.

[17] H. Zhang, W. Kang, and W. Wu, "Miniaturized dual-band SIW filters using E-shaped slotlines with controllable center frequencies," *IEEE Microwave and Wireless Components Letters*, vol. 28, no. 4, pp. 311–313, 2018.

[18] H. Zhang, W. Kang, and W. Wu, "Miniaturized dual-band differential filter based on CSRR-loaded dual-mode SIW cavity," *IEEE Microwave and Wireless Components Letters*, vol. 28, no. 10, pp. 897–899, 2018.

[19] Y. Zhu, Y. Dong, J. Bornemann, L. Gu, and D. F. Mamedes, "SIW triplets including meander-line and CRLH resonators and their applications to quasi-elliptic filters," *IEEE Transactions on Microwave Theory and Techniques*, vol. 71, no. 5, pp. 2193–2206, 2023.

[20] S. Y. Zheng, Z. L. Su, Y. M. Pan, Z. Qamar, and D. Ho, "New dual-/tri-band bandpass filters and diplexer with large frequency ratio," *IEEE Transactions on Microwave Theory and Techniques*, vol. 66, no. 6, pp. 2978–2992, 2018.

[21] X.-L. Yang, X.-W. Zhu, and X. Wang, "Dual-band substrate integrated waveguide filters with perturbed circular cavity," *IEEE Microwave and Wireless Components Letters*, vol. 32, no. 4, pp. 293–296, 2022.

[22] Q. Liu, D.-W. Zhang, K. Gong, H. Qian, W.-Z. Qu, and N. An, "Single-and dual-band bandpass filters based on multiple-mode folded substrate-integrated waveguide cavities," *IEEE Transactions on Microwave Theory and Techniques*, vol. 71, no. 12, pp. 5335–5345, 2023.

[23] X. Zhou, G. Zhang, J. Zheng et al., "Design of dual-band balanced bandpass filter based on a single substrate integrated waveguide cavity," *International Journal of RF and Microwave Computer-Aided Engineering*, vol. 32, no. 8, 2022.

[24] Y. Shen, H. Wang, W. Kang, and W. Wu, "Dual-band SIW differential bandpass filter with improved common-mode suppression," *IEEE Microwave and Wireless Components Letters*, vol. 25, no. 2, pp. 100–102, 2015.

[25] P.-L. Chi, Y.-M. Chen, and T. Yang, "Single-layer dual-band balanced substrate-integrated waveguide filtering power divider for 5G millimeter-wave applications," *IEEE Microwave and Wireless Components Letters*, vol. 30, no. 6, pp. 585–588, 2020.

[26] K. Zhou, C.-X. Zhou, H.-W. Xie, and W. Wu, "Synthesis design of SIW multiband bandpass filters based on dual-mode resonances and split-type dual- and triple-band responses," *IEEE Transactions on Microwave Theory and Techniques*, vol. 67, no. 1, pp. 151–161, 2019.

[27] K. Zhou, C.-X. Zhou, and W. Wu, "Substrate-integrated waveguide dual-mode dual-band bandpass filters with widely controllable bandwidth ratios," *IEEE Transactions on Microwave Theory and Techniques*, vol. 65, no. 10, pp. 3801–3812, 2017.

[28] Q. Lai, C. Fumeaux, W. Hong, and R. Vahldieck, "Characterization of the propagation properties of the half-mode substrate integrated waveguide," *IEEE Transactions on Microwave Theory and Techniques*, vol. 57, no. 8, pp. 1996–2004, 2009.

[29] H.-W. Xie, K. Zhou, C.-X. Zhou, W. Wu, L.-B. Zheng, and Y. Liu, "Wide-stopband substrate-integrated waveguide diplexers and dual-band bandpass filter with large frequency ratios," *International Journal of RF and Microwave Computer-Aided Engineering*, vol. 32, no. 7, 2022.

[30] D. M. Pozar, *Microwave Engineering*, Wiley, New York, NY, USA, 4th edition, 2011.

[31] J.-S. Hong and M. J. Lancaster, *Microstrip Filters for RF/Microwave Applications*, Wiley, New York, NY, USA, 2001.

[32] F. Zhu, G. Q. Luo, Z. Liao, X. W. Dai, and K. Wu, "Compact dual-mode bandpass filters based on half-mode substrate-integrated waveguide cavities," *IEEE Microwave and Wireless Components Letters*, vol. 31, no. 5, pp. 441–444, 2021.

[33] F. Zhu, G. Q. Luo, B. You, X. H. Zhang, and K. Wu, "Planar dual-mode bandpass filters using perturbed substrate-integrated waveguide rectangular cavities," *IEEE Transactions on Microwave Theory and Techniques*, vol. 69, no. 6, pp. 3048–3057, 2021.